Structure

Article

Structures of TASK-1 and TASK-3 K2P channels provide insight into their gating and dysfunction in disease

Graphical abstract

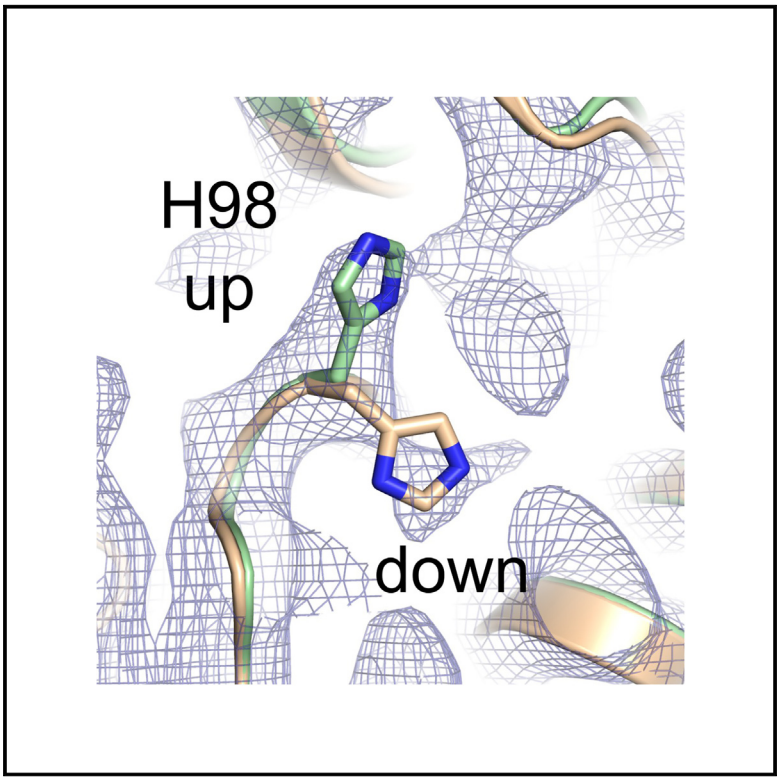

Authors

Peter Rory Hall, Thibault Jouen-Tachoire, Marcus Schewe, ..., Simon Newstead, Karin E.J. Rödström, Stephen J. Tucker

Correspondence

karin.rodstrom@bioch.ox.ac.uk (K.E.J.R.), stephen.tucker@physics.ox.ac.uk (S.J.T.)

In brief

In this study, Hall et al. determine the 3D structure of two important potassium channels, TASK-1 and TASK-3. These new structures help us to understand how these channels open and close, and why they become defective in a number of disease states.

Highlights

- Cryo-EM structures of TASK-1 and TASK-3 K^+ channels reveal a conserved lower X-gate
- H98 pH sensor residue in TASK-1 flips up at lower pH to influence the filter gate
- Structure of the *KCNK9* imprinting syndrome mutation, G236R reveals a pore constriction

Hall et al., 2025, Structure *33*, 115–122
January 2, 2025
https://doi.org/10.1016/j.str.2024.11.005

CellPress

Structure

CellPress
OPEN ACCESS

Article

Structures of TASK-1 and TASK-3 K2P channels provide insight into their gating and dysfunction in disease

Peter Rory Hall,[1,2,3,7] Thibault Jouen-Tachoire,[2,4,5] Marcus Schewe,[6] Peter Proks,[2,7] Thomas Baukrowitz,[6] Elisabeth P. Carpenter,[8] Simon Newstead,[1,5,7] Karin E.J. Rödström,[1,2,7,*] and Stephen J. Tucker[2,5,7,9,*]

[1]Department of Biochemistry, University of Oxford, Oxford, UK
[2]Clarendon Laboratory, Department of Physics, University of Oxford, Oxford, UK
[3]Scripps Institute, San Diego, CA, USA
[4]Department of Pharmacology, University of Oxford, Oxford, UK
[5]OXION Initiative in Ion Channels and Disease, University of Oxford, Oxford, UK
[6]Institute of Physiology, Kiel University, Kiel, Germany
[7]Kavli Institute for Nanoscience Discovery, University of Oxford, Oxford, UK
[8]Centre for Medicines Discovery, University of Oxford, Oxford, UK
[9]Lead contact
*Correspondence: karin.rodstrom@bioch.ox.ac.uk (K.E.J.R.), stephen.tucker@physics.ox.ac.uk (S.J.T.)
https://doi.org/10.1016/j.str.2024.11.005

SUMMARY

TASK-1 and TASK-3 are pH-sensitive two-pore domain (K2P/*KCNK*) K^+ channels. Their functional roles make them promising targets for treatment of multiple disorders including sleep apnea, pain, and atrial fibrillation. Mutations in these channels are also associated with neurodevelopmental and hypertensive disorders. A previous crystal structure of TASK-1 revealed a lower "X-gate" as a hotspot for missense gain-of-function (GoF) mutations associated with DDSA (developmental delay with sleep apnea). However, the mechanisms of gating in TASK channels are still not fully understood. Here, we resolve structures for both human TASK-1 and TASK-3 by cryoelectron microscopy (cryo-EM), as well as a recurrent TASK-3 variant (G236R) associated with *KCNK9* imprinting syndrome (KIS) (formerly known as Birk-Barel syndrome). Combined with functional studies of the X-gating mechanism, we provide evidence for how a highly conserved gating mechanism becomes defective in disease, and also provide further insight into the pathway of conformational changes that underlie the pH-dependent inhibition of TASK channel activity.

INTRODUCTION

Two-pore domain K^+ (K2P) channels are a structurally distinct subset of K^+ channels where each gene encodes a subunit with two pore-forming domains that coassemble as a dimer to create a single pseudotetrameric K^+-selective pore that spans the cell membrane.[1] Originally described as "leak" channels, K2P channels are now known to be regulated by many diverse stimuli, including multiple G-protein coupled receptor (GPCR) pathways[2] thus enabling them to integrate a range of neuronal, metabolic and cellular signaling pathways into changes in cellular electrical activity.[3,4]

In humans, K2P channels are encoded by 15 separate genes (*KCNK1–KCNK18)* and while most assemble as homomeric channels, several are able to coassemble as heteromeric channels with unique functional properties.[5,6] *KCNK3* encodes the TASK-1 K2P channel and is expressed in many chemosensitive regions of the central nervous system involved in the regulation of breathing, as well as in the lung, heart, carotid body, adrenal gland, and pulmonary arterial smooth muscle.[1,7,8] Loss-of-function (LoF) mutations in TASK-1 cause an inherited form of hypertension (pulmonary arterial hypertension [PAH]),[9,10] while *de novo* gain-of-function (GoF) mutations have recently been shown to underlie a separate disorder termed developmental delay with sleep apnea (DDSA).[11] The upregulation of atrium-selective TASK-1 currents has also been shown to contribute to the shortening of action potential duration in patients with chronic atrial fibrillation.[12] Its functional role is therefore diverse, but the expression of TASK channels in cells and tissues involved in both the control of respiratory drive and in mechanical ventilation, as well as its genetic association with DDSA, have clearly implicated TASK-1 as a target for the treatment of sleep apnea, and in a recent clinical trial a novel TASK channel inhibitor was found to reduce sleep apnea severity in patients with severe obstructive sleep apnea.[13]

The related TASK-3 channel is encoded by *KNCK9* and shares 54% overall amino acid identity with TASK-1 and 80% identity within the pore-forming transmembrane regions. TASK-3 is

also expressed widely throughout the CNS and several peripheral tissues. Furthermore, in places where both TASK-1 and TASK-3 are coexpressed, e.g., in the carotid body, heteromeric TASK-1/TASK-3 channels appear to coassemble to form the physiologically relevant channel subtype in those cells.[5,6,14]

KCNK9 imprinting syndrome (KIS) is a rare neurodevelopmental disorder, previously referred to as Birk-Barrel syndrome. KIS is primarily characterized by LoF mutations in the maternal copy of the gene, with the majority of patients possessing a single G236R mutation.[15] More recently, GoF mutations have also been associated with this disorder,[16] but the underlying molecular mechanisms behind this genotype-phenotype correlation remain unclear and can often be complicated by imprinting and/or mosaicism. Interestingly, TASK-3 has also been shown to be expressed in certain nociceptive sensory neurons and TASK-3 activators have been shown to display potent analgesic effects in a variety of rodent pain models suggesting this channel as a potential target for the treatment of pain.[17]

In a recent study, we determined an X-ray crystal structure of TASK-1 in complex with a compound class of TASK-1 inhibitors developed for the treatment of sleep apnea.[18] This structure also revealed several unique features of TASK-1, including a lower "X-gate," a structural motif involving constriction of the M4 helices that controls opening and closing of the channel pore. The X-gate and surrounding region also appears to be a hotspot for GoF mutations underlying DDSA by creating channels that have both a higher open probability and that are resistant to GPCR-mediated inhibition.[11]

The extracellular H^+ sensitivity of TASK channels is also an important and physiologically relevant feature with their name originally derived from their acid sensitivity.[8] TASK-1 and TASK-3 channels have pK_a values of ~7.4 and 6.7, respectively, thus permitting their activity to be finely tuned by changes in extracellular H^+ concentrations within the physiological range.[19] Previous studies have identified the pH-sensor as H98 positioned adjacent to the first selectivity filter (SF) motif (^{93}TIGYGH^{98}).[20] The first insights into the mechanism of gating have been provided by cryoelectron microscopy (cryo-EM) structures of the related TWIK-1 channel that also possesses a histidine pH-sensor in a similar position within the filter motif[21] and more recently by a structure of TASK-3,[22] but the precise mechanism by which protonation of H98 influences channel gating in TASK channels has not been fully elucidated. It is known that even relatively small structural rearrangements within the pore-forming loops control a "C-type" or inactivation gate within the SF of many K2P channels and similar changes may therefore also be sufficient to regulate gating in TASK channels.[23–26]

However, for any such SF gate to function, the lower X-gate must also open, and in many K^+ channels such gates are allosterically coupled.[27–29] In TASK-1 we have previously shown that mutations that affect X-gating can also influence activation by external H^+, but that they do not prevent inhibition. This suggests that if such coupling exists between these gates, then it may be relatively weak.[11] However, without more detailed structural or functional information, such mechanisms remain difficult to determine. Likewise, without more structural information, the effects of disease-causing mutations remain difficult to interpret as well as impacting the rational design of better therapeutics that target these channels.

To address these issues, we have used single particle cryo-EM to solve the structure of TASK-3 with and without the most frequent KIS mutation (G236R) as well as a structure of TASK-1, and we use functional studies to demonstrate that the X-gating mechanism is conserved in TASK-3. Importantly, these structures indicate how the pH-sensor in TASK-1 channels may begin to move in response to protonation to control channel gating, and also how the X-gate may begin to open. We discuss how these movements relate to other structures of TASK-3 recently resolved by cryo-EM at different pH values[22] and how these various new structures provide further insight into the gating mechanism of TASK channels and their associated channelopathies, as well as expanding the structural landscape of TASK K2P channels as druggable targets.

RESULTS AND DISCUSSION

Cryo-EM structure of TASK-1

The previous crystal structure of TASK-1 revealed a lower X-gate that was also seen in the two inhibitor-bound structures resolved in that study.[18] However, the contacts required for crystallization occasionally influence structures to produce non-native conformations. An advantage of single particle cryo-EM is that additional native conformations can often be resolved. We therefore determined a cryo-EM structure using human TASK-1 protein identical to that used previously for crystallization (Met1-Glu259).

We were able to resolve this structure to 3.1 Å resolution (Figure 1, Table S1 and Figure S1) and the overall structure was found to be consistent with previous biochemical and crystallographic structures of TASK-1. Superimposition of the cryo-EM and crystal structures revealed very similar conformations (Figures 1A–1C). The channel forms a domain-swapped homodimer with four transmembrane helices (M1–M4) in each subunit, a pseudotetrameric SF similar to other K2Ps, and an extracellular Cap domain that lacks the intermolecular disulfide bridge between chains found in most other K2Ps.[30] Even though the distal C-terminus beyond A251 is not resolved as well as in the crystal structure, the architecture of the X-gate (^{243}VLRFMT^{248}) is clearly visible and conserved, thus confirming the structural integrity of this gating motif. Cholesterol hemisuccinate was also identified bound to the same external clefts as seen in the TASK-1 crystal structure, i.e., next to the X-gate between the M1, M4, and M2 helices with a second site in a higher cavity along the M4 helices (Figure S1D).

TASK-1 pH-Sensor

Both TASK-1 and TASK-3 channels are sensitive to inhibition by extracellular H^+ within the physiological range. The crystal structure of TASK-1 was originally solved at pH 8.5 with the pH-sensor, H98 presumably in the activated state where it points down to stabilize the region behind the filter via H-bond formation involving a water molecule and other side-chains within this region[18] (Figure 1D). Similar networks of interactions have also been observed in other K^+ channels stabilizing their K^+ selective filters in active, conductive conformations.[27] The H98 side chain is also adjacent to two glutamines (Q77 and Q209) at pH 8.5 in the crystal structure

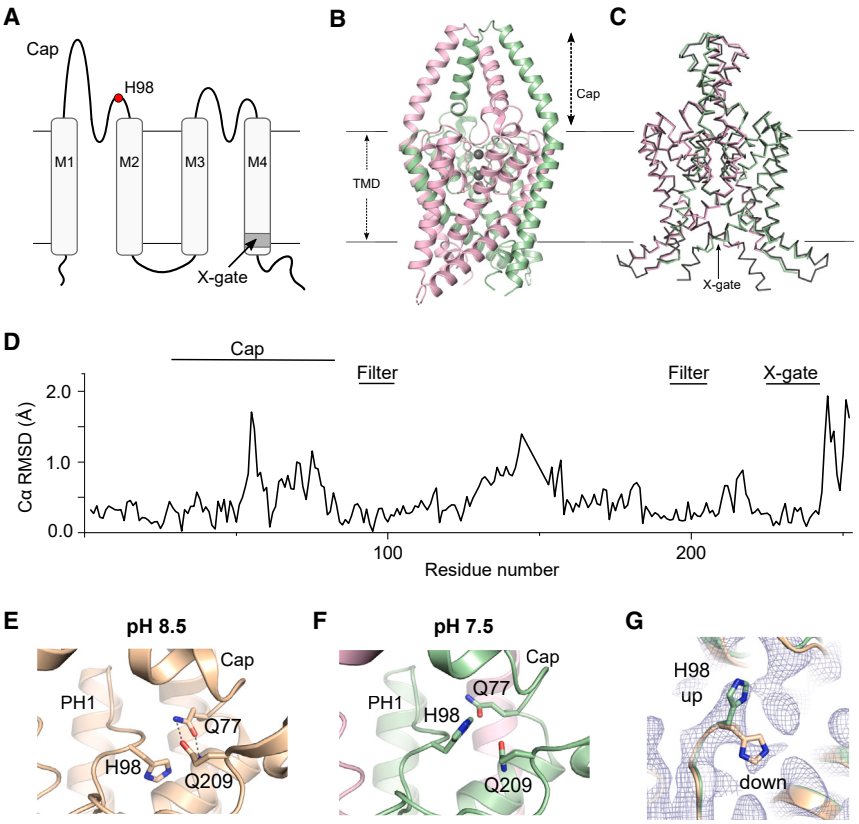

Figure 1. Cryo-EM structure of TASK-1

(A) Cartoon showing the topology of a single TASK-1 subunit indicating the relative position of the pH-sensor, H98 (red dot), the M1–M4 transmembrane helices, and the X-gate.

(B) Cryo-EM structure of TASK-1, with chain A in green and chain B in pink.

(C) Superimposition of this TASK-1 cryo-EM structure and the TASK-1 crystal structure 6RV2 (dark gray).

(D) RMSD plot of the TASK-1 cryo-EM structure compared to the crystal structure (6RV2).

(E) H98 in TASK-1 at pH 8.5 from PDB: 6RV2.

(F) Conformation of H98 at pH 7.5 as determined in this cryo-EM structure. In this structure the H-bonding between Q77 and Q209 is disrupted.

(G) Dual rotamer density of H98 clearly visible in the map, with the X-ray structure (PDB: 6RV2) in beige superimposed on the TASK-1 cryoEM structure shown in green.

conformation with Q77 H-bonding with Q209, and mutations in this network of residues have been shown to alter TASK-1 pH sensitivity.[18]

Interestingly, despite the high degree of structural alignment in most other regions of the structure, the conformation of this pH-sensor in the new cryo-EM structure, determined at pH 7.5, is markedly different from that previously found at pH 8.5 (Figure 1E). At pH 7.5, H98 adopts an alternative rotamer conformation and there is a disruption of the hydrogen bonds between Q77 and Q209. There is no direct comparison available for an equivalent cryo-EM structure of TASK-1 at higher pH, however, some density is still also observed for the downward rotamer (Figure 1F). This is consistent with the pKa for TASK-1 pH sensitivity and indicates that at pH 7.5 both conformations may exist. This therefore suggests that the first stages of pH sensitivity involve protonation of H98 that induces an upwards movement and disruption of the network of interactions between H98-Q77-Q209.

Cryo-EM structure of TASK-3

To investigate the structure of the related human TASK-3 channel we used an almost identical expression construct (Met1-Glu259) combined with a similar structural approach to determine a structure to 3.3 Å resolution (Figure 2, Table S1 and Figure S2). In TASK-3, the X-gate sequence motif (^{243}VLRFLT^{248}) is slightly different from that of TASK-1 (^{243}VLRFMT^{248}). The overall fold of this TASK-3 structure is very similar to that of TASK-1 and almost identical to other structures of TASK-3 recently resolved by cryo-EM.[22]

Together, these structures therefore confirm that TASK-3 possesses a structurally conserved lower X-gate motif where the distal end of the M4 helices kink and block the entrance to the inner cavity (Figures 2A–2E). Similar to TASK-1, cholesteryl hemisuccinate was also found bound to the same regions next to the X-gate between the M1, M2, and M4 helices, with a second site in a higher cavity along the M4 helices (Figure S2D). The pH-sensor (H98) is also found within the first filter motif (^{93}TIGYGH^{98}) in TASK-3, but in this structure solved at pH 7.5, only the downward facing rotamer was observed (Figure 2D). This is consistent with the slightly reduced H^+ sensitivity of TASK-3 that is considerably more active at pH 7.5 than TASK-1 and so would be expected to be in the stable, conductive conformation.

The orientation of H98 is also consistent with structures of TASK-3 recently resolved by Lin et al. at pH 7.4.[22] However, in that study, the authors also solved a structure of TASK-3 at pH 6.0 that revealed much larger rearrangements of the filter backbone in this region. Intriguingly, these larger changes at pH 6.0 could only be observed at low concentrations of K^+, yet they share some similarity with a structure of TWIK-1 solved at pH 5.5 that suggest that protonation of a histidine at this position adjacent to the filter might induce a much larger rearrangement of the backbone to constrict the outermost part of the filter itself.[21]

Conserved functional role of the X-gate in TASK-3

As found in TASK-1, the residues that surround the X-gate in TASK-3 are also involved in inter- and/or intra-subunit interactions known to influence channel gating in both channels.[31] For example, in a recent study, a number of disease-causing mutations in TASK-1 were shown to destabilize the X-gate, increase channel open probability (P_o) and reduce GPCR-sensitivity.[11] To examine whether this X-gating mechanism is functionally conserved in TASK-3, we therefore examined the activity of several equivalent mutations in TASK-3. We found that, similar to their activatory effect in TASK-1, the GoF DDSA mutations

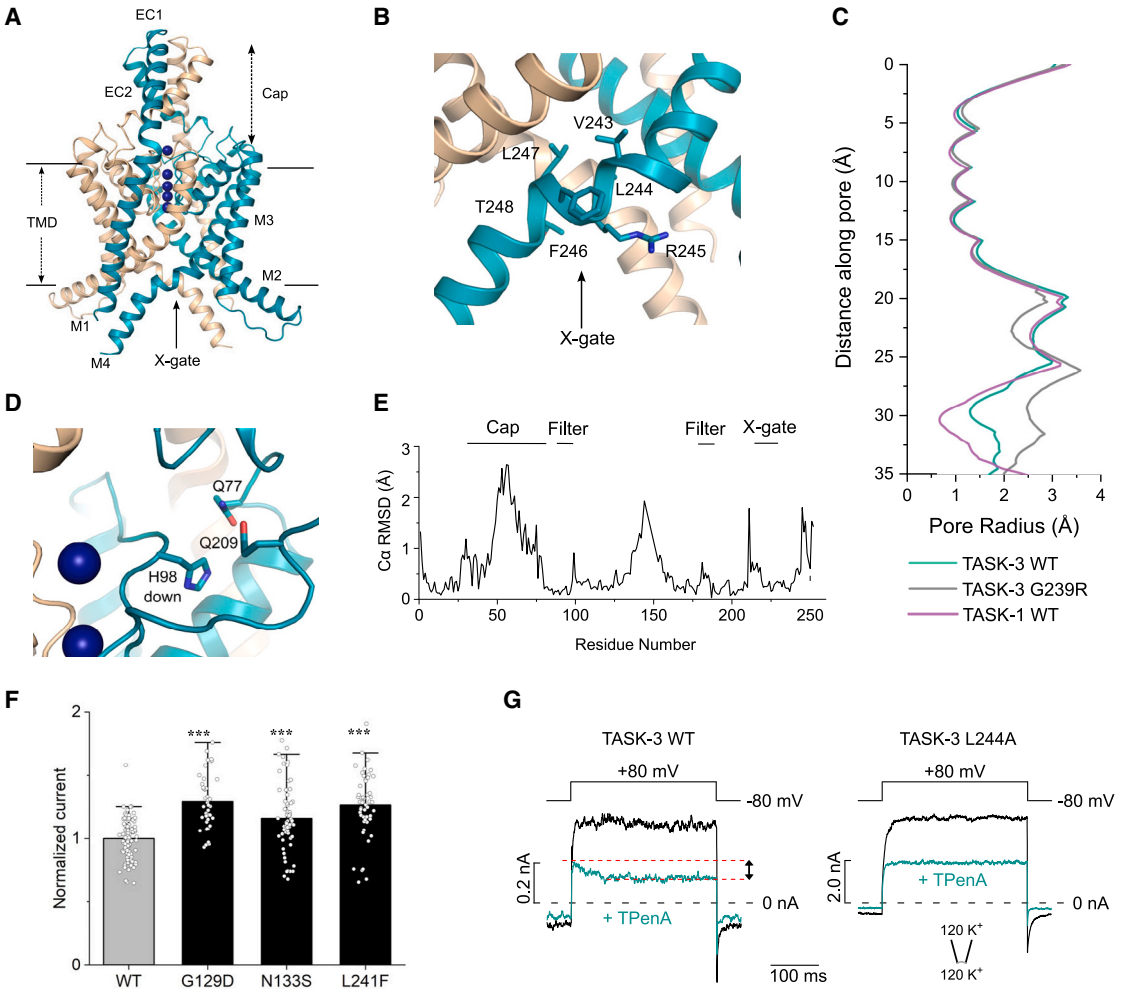

Figure 2. Cryo-EM structure of TASK-3

(A) Cartoon showing the structure of TASK-3, with chain A in gold and chain B in teal.

(B) The X-gate environment of TASK-3.

(C) Pore radius profile of WT TASK-3 and the other structures determined in this study.

(D) H98 downward conformation.

(E) RMSD plot of TASK-3 versus TASK-1.

(F) Whole-cell recordings of WT TASK-3 ($n = 95$) and TASK-3 with "DDSA" mutations: G129D ($n = 42$), N133S ($n = 60$), and L241F ($n = 51$). The error bars represent the mean ± SEM. ***$p < 0.0001$.

(G) Current-voltage responses measured in inside-out patches from *Xenopus* oocytes expressing WT or L244A mutant TASK-3 channels in symmetrical high K^+ at pH 7.4 in the absence (black) and in the presence of 1 μM TPenA (teal). Currents were elicited by the voltage steps indicated above the traces. The dotted red line indicates the extent of block by TPenA seen in WT TASK-1 when the X-gate opens upon voltage-activation. This is not seen in the more active L244A mutant channel. The example measurements shown here for WT and mutant channels were repeated with similar results ($n = 6$).

(G129D, N133S, and L241F) that destabilize the X-gate in TASK-1 also increased whole-cell currents for TASK-3 (Figure 2F). The magnitude of this increase was less than that found in TASK-1, but this is probably due to the intrinsically higher open probability of wild-type (WT) TASK-3 to begin with. Indeed, it has previously been shown that a similar mutation of N133 in TASK-3 directly increases single channel open probability[32] therefore supporting our observations that these mutations have an activatory effect due to the overall conservation of the X-gating motif in TASK-3.

Interestingly, we also found that functional measurements of macroscopic WT TASK-3 currents in excised patches using the universal K^+ channel blocker tetrapentylammonium (TPenA) showed a slow component of inhibition (about 30% of the total block) upon voltage activation. This block resembles the time course of inhibition seen with similar slow open channel blockersin classical voltage-gated K^+ channels.[33] Furthermore, for TASK-3 channels, it was recently shown that voltage activation is achieved through a voltage-dependent SF gate.[28] These results therefore suggest that voltage activation also opens the lower X-gate in TASK-3, allowing TPenA to reach its binding site in the inner cavity and is comparable to the mechanism recently described for the related TALK-2 K2P channel.[29] To further examine this mechanism for TASK-3, we used a mutation at the X-gate (L244A)[18]

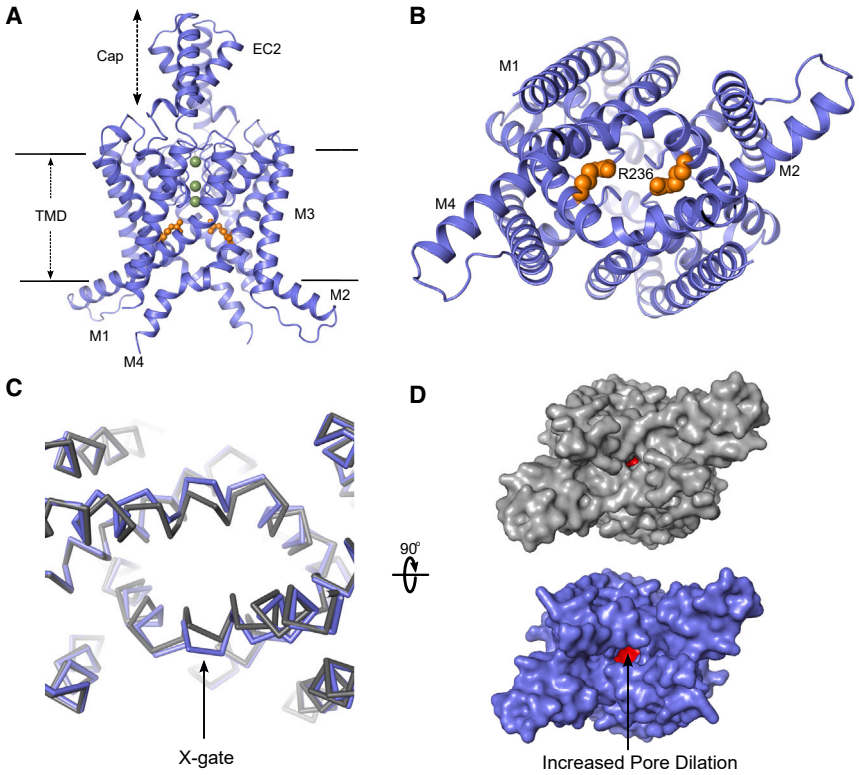

Figure 3. Cryo-EM structure of TASK-3 G236R

(A) Cartoon showing the structure of TASK-3 G236R, with the two chains of the homodimer shown in blue.

(B) The position of R236 within the inner cavity is shown as orange VdW spheres.

(C and D) Overlay of TASK-3 (gray) and TASK-3 G236R (blue) highlighting the additional movement in the X-gate and increased pore dilation in that region (expanded in D).

that has previously been shown to open the X-gate in TASK-1 and therefore expected to reduce this effect. Consistent with this, we found that the L244A mutation abolished this time-dependent component of blocker inhibition (Figure 2G). This not only supports a clear role for the X-gate in the gating of TASK-3 channels, but also highlights a degree of allosteric coupling between the filter and X-gate in these channels.

Structure of the G236R TASK-3 mutation associated with KCNK9 imprinting syndrome

Both GoF and LoF mutations in TASK-3 lead to the neurodevelopmental disorder, KIS[16]. However, the most frequent mutation associated with this disorder is G236R on the M4 helix that results in significantly reduced channel activity. This mutation was not only the first to be reported, but also appears to be the most common recurrent missense variant associated with the disorder. The precise mechanism by which this LoF mutation reduces channel activity is unclear because the mutant channels are not completely inactive and can be partially reactivated by TASK-3 activators such as flufenamic acid and terbinafine.[34,35] We therefore used a similar approach to determine the structure of the G236R mutant channel to 2.5 Å resolution (Figure 3, Table S1 and Figure S3). Overall, the structure of this mutant channel was very similar to WT TASK-3, but with the mutant arginine side-chain from each monomer directly facing into the inner cavity to line the pore (Figure 3B).

Intriguingly, it has also previously been shown in mutagenesis studies that introduction of a negative charge into this position (G236D) produces an activatory effect,[36] and so it is likely that these positive charges directly interfere with the movement of K^+ to reduce permeation through the channel thereby explaining the LoF phenotype associated with this mutation. In addition, these two arginine residues are in relatively close proximity to each other within the inner cavity and we observed small changes in the local environment of the X-gate (Figures 3C and 3D). This movement causes the M4 helices to move apart in a direction similar to that seen in simulations of pore-opening in TASK-1 mutant channels,[11] and so may provide insight into the mechanisms that allow the aperture within the X-gate to expand during channel opening.

Summary and conclusions

Overall, our results provide further insight into the structure of both TASK-1 and TASK-3 channels and demonstrate that the X-gating mechanism is a highly conserved structural gating motif within the TASK channel family that, like many other K^+ channels, also exhibits a degree of allosteric coupling between the lower gate and the filter gate. The extent of this coupling and the precise mechanisms of pH-sensing remain to be determined, but the alternate conformations of the H98 residue we observe in TASK-1 now provides evidence for the first structural changes that may occur after protonation of this residue, and suggest how flipping of the H98 side-chain may impact the structural dynamics of this region and gating within the filter itself (Figure 4).

A structure of TWIK-1 at pH 5.5 reveals much larger rearrangements of the backbone that constrict the outermost part of the filter itself (Figure 4D), and another, very recent cryo-EM structure of TASK-3 was solved at pH 6.0 with low K^+ (5 mM) also included much larger rearrangements of the filter backbone in this region[22] (Figures 4B and 4C). In the pH 6.0 structure of TASK-3, H98 has reoriented, but is not in a fully upward conformation compared to H98 in the TASK-1 structure we present here at pH 7.5 (Figure 4A). Other key residues within the filter of TASK-3 also undergo large rearrangements at pH 6.0 and low K^+, but intriguingly these changes were not seen in high K^+ and include a major reorientation of Y96 in the P1 filter motif from its position behind the filter to restrict the pore opening (Figure 4C).

However, it has been shown in other K2P channels, and in other K^+ channels, that only small structural movements in the filter are required to affect the conformational dynamics of this region and influence K^+ permeation.[25–28] The small movements and changes in the H-bonding network we observe

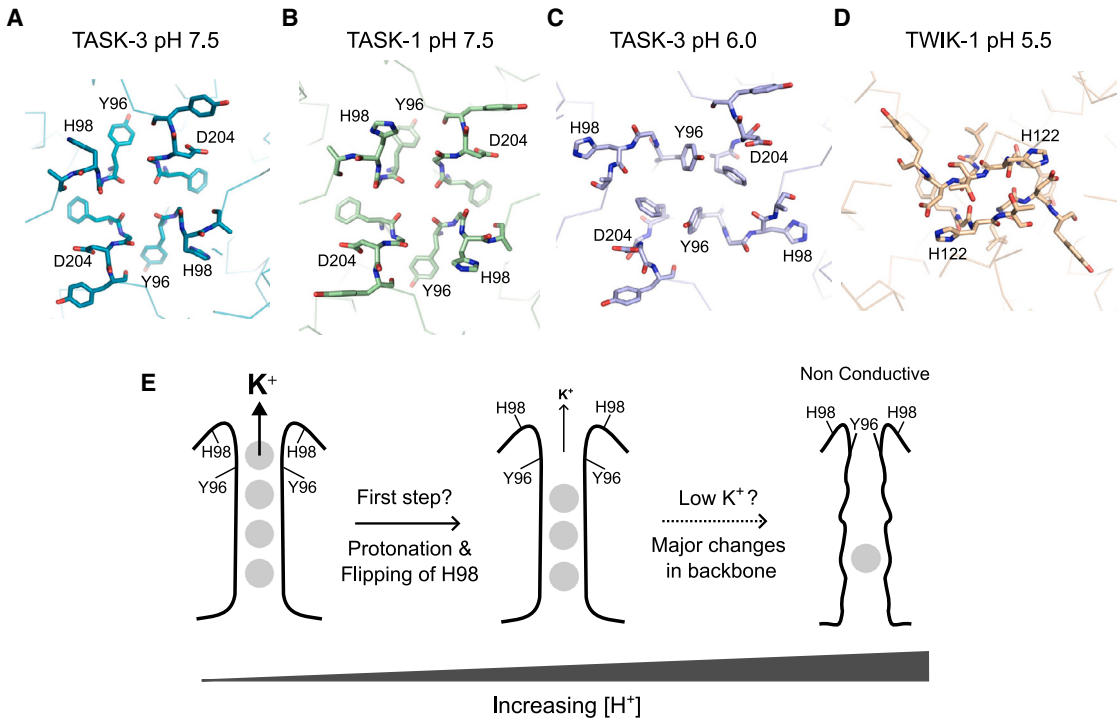

Figure 4. Comparison of pH-dependent changes in the filters of TASK and TWIK channels

(A) Top down view of TASK-3 at pH 7.5 (this study), H98 pointing down behind the filter and Y96 of the GYG motif is in its canonical orientation.

(B) TASK-1 at pH 7.5 (this study), H98 pointing up but with Y96 still in its canonical position.

(C) TASK-3 at pH 6.0 and low K^+ (PDB ID 8K1Q), H98 reoriented, with Y96 and F202 pointing upwards blocking the pore.

(D) For comparison, TWIK-1 at pH 5.5 (PDB ID 7SK1) is also shown with major rearrangement and distortion of the filter loop that restricts the pore, pH-sensor H122 is also pointing up.

(E) Schematic side view of the filter region summarizing the sequence of possible events involved pH-dependent gating of TASK channels. Initially, at high pH the filter is in a canonical, fully conductive conformation represented by full ion occupancy of the filter. In response to increasing $[H^+]$, the first step involves protonation of H98 and upwards flipping of this side chain. Consequent changes in H-bonding behind the filter and the structural dynamics of this region will begin to reduce K^+ permeation and may represent the first step in pH-gating. However, at even lower pH and low $[K^+]$, more dramatic structural changes have also been observed that switch the backbone of the filter into a non-canonical conformation with Y96 pointing inwards and upwards.[22] Whether these larger structural changes are necessary to gate the filter and reduce channel activity remains to be determined.

within the loops that connect to and support the SF may therefore influence the dynamics of the filter backbone itself, but whether this is sufficient to affect permeation by itself remains to be determined and instead may just represent the first stage of larger movements that occur at more extreme pH values (Figure 4E). It will also be interesting to see if other changes occur in the structure of the filter of TASK-1 at lower pH and/or low K^+ concentrations and whether larger changes are necessary to gate the channel. The role of these different conformational changes and how their relative dynamics influence the rate of K^+ permeation through the filter therefore remains to be determined.

Either way, it is clear that all of these new structures of TASK-1 and TASK-3 now expand the conformational landscape available for TASK channels as druggable targets and increase our insight into the mechanism of pH-sensing as well as a potential mechanism for coupling between the filter and the X-gate in TASK channels. The positively charged lining of the pore in the recurrent disease-causing G236R TASK-3 mutant also provides a clear structural explanation for the LoF phenotype associated with this mutation in KIS, and when combined with more structural information for WT TASK-3 now provides a robust structural framework for the development of activators against TASK-3 and other disease-associated mutations.

RESOURCE AVAILABILITY

Lead contact

Requests for further information and resources should be directed to and will be fulfilled by the lead contact, Stephen J. Tucker (stephen.tucker@physics.ox.ac.uk).

Materials availability

Any unique reagents produced during this study can be obtained from the lead contact upon reasonable request.

Data and code availability

The atomic coordinates for the models in this study have been deposited in the Protein DataBank (PDB) with the accession numbers 9G9V, 9G9W, and 9G9X. Coulomb potential maps have been deposited in the EMDB database, under the following accession codes: EMD-51158, EMD-51159, and EMD-51160. They are publicly available as of the date of publication. Accession codes are also listed in the key resources table. All data created or analyzed during this research are provided within the manuscript and supplementary materials.

These data do not report original code. Any additional information required to reanalyze the data reported in this paper is available from the lead contact upon request.

ACKNOWLEDGMENTS

This work was supported by grants from the Biotechnology and Biological Sciences Research Council and Medical Research Council to S.J.T., S.N., and K.E.J.R. (BB/T002018/1, BB/S008608/1 and MR/W017741/1) and from the Deutsche Forschungsgemeinschaft to M.S. (SCHE 2112/1–2) and T.B. (BA 1793/6-2) as part of the Research Unit FOR2518, DynIon. We would also like to acknowledge contributions from David Speedman and other members of the Centre for Medicines Discovery, Oxford during the early stages of this project and to Kathryn Smith for her assistance. Electron microscopy was provided through the Central Oxford Structural Molecular Imaging Centre (COSMIC).

AUTHOR CONTRIBUTIONS

S.J.T., S.N., P.R.H., and K.E.J.R. conceived/designed the principal elements of the study. All authors generated, analyzed or interpreted data or generated materials. P.R.H., S.J.T., and K.E.J.R drafted the manuscript and all authors contributed to the final version.

DECLARATION OF INTERESTS

The authors declare no competing interests.

STAR★METHODS

Detailed methods are provided in the online version of this paper and include the following:

- KEY RESOURCES TABLE
- EXPERIMENTAL MODEL AND STUDY PARTICIPANT DETAILS
- METHOD DETAILS
  - Cloning and expression of TASK-3$^{Met1–Glu259}$ for structural studies
  - Purification of TASK-1 and TASK-3
  - Cryo-EM grid preparation and data collection
  - Image processing
  - Model building, fitting and refinement
  - Electrophysiology
- QUANTIFICATION AND STATISTICAL ANALYSIS

SUPPLEMENTAL INFORMATION

Supplemental information can be found online at https://doi.org/10.1016/j.str.2024.11.005.

Received: August 6, 2024
Revised: October 16, 2024
Accepted: November 8, 2024
Published: December 4, 2024

REFERENCES

1. Enyedi, P., and Czirják, G. (2010). Molecular background of leak K+ currents: two-pore domain potassium channels. Physiol. Rev. *90*, 559–605.
2. Mathie, A. (2007). Neuronal two-pore-domain potassium channels and their regulation by G protein-coupled receptors. J. Physiol. *578*, 377–385.
3. Natale, A.M., Deal, P.E., and Minor, D.L., Jr. (2021). Structural insights into the mechanisms and pharmacology of K2P potassium channels. J. Mol. Biol. *433*, 166995.
4. Niemeyer, M.I., Cid, L.P., González, W., and Sepúlveda, F.V. (2016). Gating, Regulation, and Structure in K2P K+ Channels: In Varietate Concordia? Mol. Pharmacol. *90*, 309–317.
5. Czirjak, G., and Enyedi, P. (2002). Formation of functional heterodimers between the TASK-1 and TASK-3 two-pore domain potassium channel subunits. J. Biol. Chem. *277*, 5426–5432.
6. Khoubza, L., Chatelain, F.C., Feliciangeli, S., Lesage, F., and Bichet, D. (2021). Physiological roles of heteromerization: focus on the two-pore domain potassium channels. J. Physiol. *599*, 1041–1055.
7. Olschewski, A., Veale, E.L., Nagy, B.M., Nagaraj, C., Kwapiszewska, G., Antigny, F., Lambert, M., Humbert, M., Czirják, G., Enyedi, P., and Mathie, A. (2017). TASK-1 (KCNK3) channels in the lung: from cell biology to clinical implications. Eur. Respir. J. *50*, 1700754.
8. Duprat, F., Lesage, F., Fink, M., Reyes, R., Heurteaux, C., and Lazdunski, M. (1997). TASK, a human background K+ channel to sense external pH variations near physiological pH. EMBO J. *16*, 5464–5471.
9. Jouen-Tachoire, T.R.H., Tucker, S.J., and Tammaro, P. (2021). Ion channels as convergence points in the pathology of pulmonary arterial hypertension. Biochem. Soc. Trans. *49*, 1855–1865.
10. Ma, L., Roman-Campos, D., Austin, E.D., Eyries, M., Sampson, K.S., Soubrier, F., Germain, M., Trégouët, D.A., Borczuk, A., Rosenzweig, E.B., et al. (2013). A novel channelopathy in pulmonary arterial hypertension. N. Engl. J. Med. *369*, 351–361.
11. Sormann, J., Schewe, M., Proks, P., Jouen-Tachoire, T., Rao, S., Riel, E.B., Agre, K.E., Begtrup, A., and Dean, J. (2022). Descartes M., et al. Gain-of-function mutations in KCNK3 cause a developmental disorder with sleep apnea. Nat. Genet. *54*, 1534–1543.
12. Schmidt, C., Wiedmann, F., Voigt, N., Zhou, X.B., Heijman, J., Lang, S., Albert, V., Kallenberger, S., Ruhparwar, A., Szabó, G., et al. (2015). Upregulation of K(2P)3.1 K+ Current Causes Action Potential Shortening in Patients With Chronic Atrial Fibrillation. Circulation *132*, 82–92.
13. Osman, A.M., Toson, B., Naik, G.R., Mukherjee, S., Delbeck, M., Hahn, M., Muller, T., Weimann, G., and Eckert, D.J. (2024). A novel TASK channel antagonist nasal spray reduces sleep apnea severity in physiological responders: a randomized, blinded, trial. Am. J. Physiol. Heart Circ. Physiol. *326*, H715–H723.
14. Kim, D., Cavanaugh, E.J., Kim, I., and Carroll, J.L. (2009). Heteromeric TASK-1/TASK-3 is the major oxygen-sensitive background K+ channel in rat carotid body glomus cells. J. Physiol. *587*, 2963–2975.
15. Barel, O., Shalev, S.A., Ofir, R., Cohen, A., Zlotogora, J., Shorer, Z., Mazor, G., Finer, G., Khateeb, S., Zilberberg, N., and Birk, O.S. (2008). Maternally inherited Birk Barel mental retardation dysmorphism syndrome caused by a mutation in the genomically imprinted potassium channel KCNK9. Am. J. Hum. Genet. *83*, 193–199.
16. Cousin, M.A., Veale, E.L., Dsouza, N.R., Tripathi, S., Holden, R.G., Arelin, M., Beek, G., Bekheirnia, M.R., Beygo, J., Bhambhani, V., et al. (2022). Gain and loss of TASK3 channel function and its regulation by novel variation cause KCNK9 imprinting syndrome. Genome Med. *14*, 62.
17. Liao, P., Qiu, Y., Mo, Y., Fu, J., Song, Z., Huang, L., Bai, S., Wang, Y., Zhu, J.J., Tian, F., et al. (2019). Selective activation of TWIK-related acid-sensitive K(+) 3 subunit-containing channels is analgesic in rodent models. Sci. Transl. Med. *11*, eaaw8434.
18. Rodstrom, K.E.J., Cloake, A., Sörmann, J., Baronina, A., Smith, K.H.M., Pike, A.C.W., Ang, J., Proks, P., Schewe, M., Holland-Kaye, I., et al. (2020). A lower X-gate in TASK channels traps inhibitors within the vestibule. Nature *582*, 443–447.
19. Bayliss, D.A., Barhanin, J., Gestreau, C., and Guyenet, P.G. (2015). The role of pH-sensitive TASK channels in central respiratory chemoreception. Pflugers Arch. *467*, 917–929.
20. Rajan, S., Wischmeyer, E., Xin Liu, G., Preisig-Müller, R., Daut, J., Karschin, A., and Derst, C. (2000). TASK-3, a novel tandem pore domain acid-sensitive K+ channel. An extracellular histiding as pH sensor. J. Biol. Chem. *275*, 16650–16657.
21. Turney, T.S., Li, V., and Brohawn, S.G. (2022). Structural Basis for pH-gating of the K(+) channel TWIK1 at the selectivity filter. Nat. Commun. *13*, 3232.

22. Lin, H., Li, J., Zhang, Q., Yang, H., and Chen, S. (2024). C-type inactivation and proton modulation mechanisms of the TASK3 channel. Proc. Natl. Acad. Sci. USA *121*, e2320345121.

23. Bagriantsev, S.N., Peyronnet, R., Clark, K.A., Honoré, E., and Minor, D.L., Jr. (2011). Multiple modalities converge on a common gate to control K2P channel function. EMBO J. *30*, 3594–3606.

24. Piechotta, P.L., Rapedius, M., Stansfeld, P.J., Bollepalli, M.K., Ehrlich, G., Andres-Enguix, I., Fritzenschaft, H., Decher, N., Sansom, M.S.P., Tucker, S.J., and Baukrowitz, T. (2011). The pore structure and gating mechanism of K2P channels. EMBO J. *30*, 3607–3619.

25. Lolicato, M., Natale, A.M., Abderemane-Ali, F., Crottès, D., Capponi, S., Duman, R., Wagner, A., Rosenberg, J.M., Grabe, M., and Minor, D.L., Jr. (2020). K2P channel C-type gating involves asymmetric selectivity filter order-disorder transitions. Sci. Adv. *6*, eabc9174.

26. Brennecke, J.T., and de Groot, B.L. (2018). Mechanism of Mechanosensitive Gating of the TREK-2 Potassium Channel. Biophys. J. *114*, 1336–1343.

27. McCoy, J.G., and Nimigean, C.M. (2012). Structural correlates of selectivity and inactivation in potassium channels. Biochim. Biophys. Acta *1818*, 272–285.

28. Kopec, W., Rothberg, B.S., and de Groot, B.L. (2019). Molecular mechanism of a potassium channel gating through activation gate-selectivity filter coupling. Nat. Commun. *10*, 5366.

29. Neelsen, L.C., Riel, E.B., Rinné, S., Schmid, F.R., Jürs, B.C., Bedoya, M., Langer, J.P., Eymsh, B., Kiper, A.K., Cordeiro, S., et al. (2024). Ion occupancy of the selectivity filter controls opening of a cytoplasmic gate in the K2P channel TALK-2. Nat. Commun. *15*, 7545.

30. Goldstein, M., Rinné, S., Kiper, A.K., Ramírez, D., Netter, M.F., Bustos, D., Ortiz-Bonnin, B., González, W., and Decher, N. (2016). Functional mutagenesis screens reveal the 'cap structure' formation in disulfide-bridge free TASK channels. Sci. Rep. *6*, 19492.

31. Talley, E.M., and Bayliss, D.A. (2002). Modulation of TASK-1 (Kcnk3) and TASK-3 (Kcnk9) potassium channels: volatile anesthetics and neurotransmitters share a molecular site of action. J. Biol. Chem. *277*, 17733–17742.

32. Ashmole, I., Vavoulis, D.V., Stansfeld, P.J., Mehta, P.R., Feng, J.F., Sutcliffe, M.J., and Stanfield, P.R. (2009). The response of the tandem pore potassium channel TASK-3 (K(2P)9.1) to voltage: gating at the cytoplasmic mouth. J. Physiol. *587*, 4769–4783.

33. Choi, K.L., Mossman, C., Aubé, J., and Yellen, G. (1993). The internal quaternary ammonium receptor site of Shaker potassium channels. Neuron *10*, 533–541.

34. Veale, E.L., Hassan, M., Walsh, Y., Al-Moubarak, E., and Mathie, A. (2014). Recovery of current through mutated TASK3 potassium channels underlying Birk Barel syndrome. Mol. Pharmacol. *85*, 397–407.

35. Wright, P.D., Veale, E.L., McCoull, D., Tickle, D.C., Large, J.M., Ococks, E., Gothard, G., Kettleborough, C., Mathie, A., and Jerman, J. (2017). Terbinafine is a novel and selective activator of the two-pore domain potassium channel TASK3. Biochem. Biophys. Res. Commun. *493*, 444–450.

36. Chokshi, R.H., Larsen, A.T., Bhayana, B., and Cotten, J.F. (2015). Breathing Stimulant Compounds Inhibit TASK-3 Potassium Channel Function Likely by Binding at a Common Site in the Channel Pore. Mol. Pharmacol. *88*, 926–934.

37. Caesar, J., Reboul, C.F., Machello, C., Kiesewetter, S., Tang, M.L., Deme, J.C., Johnson, S., Elmlund, D., Lea, S.M., and Elmlund, H. (2020). SIMPLE 3.0. Stream single-particle cryo-EM analysis in real time. J. Struct. Biol. *4*, 100040.

38. Punjani, A., Rubinstein, J.L., Fleet, D.J., and Brubaker, M.A. (2017). cryoSPARC: algorithms for rapid unsupervised cryo-EM structure determination. Nat. Methods *14*, 290–296.

39. Zivanov, J., Nakane, T., Forsberg, B.O., Kimanius, D., Hagen, W.J., Lindahl, E., and Scheres, S.H. (2018). New tools for automated high-resolution cryo-EM structure determination in RELION-3. Elife *7*, e42166.

40. Asarnow, D., Palovcak, E., and Cheng, Y. (2019). UCSF Pyem v0.5 (Zenodo). https://doi.org/10.5281/zenodo.3576630.

41. Zhu, J., Zhang, Q., Zhang, H., Shi, Z., Hu, M., and Bao, C. (2023). A minority of final stacks yields superior amplitude in single-particle cryo-EM. Nat. Commun. *14*, 7822.

42. Emsley, P., Lohkamp, B., Scott, W.G., and Cowtan, K. (2010). Features and development of Coot. Acta Crystallogr. D Biol. Crystallogr. *66*, 486–501.

43. Adams, P.D., Afonine, P.V., Bunkóczi, G., Chen, V.B., Davis, I.W., Echols, N., Headd, J.J., Hung, L.W., Kapral, G.J., Grosse-Kunstleve, R.W., et al. (2010). PHENIX: a comprehensive Python-based system for macromolecular structure solution. Acta Crystallogr. D Biol. Crystallogr. *66*, 213–221.

44. Croll, T.I. (2018). ISOLDE: a physically realistic environment for model building into low-resolution electron-density maps. Acta Crystallogr. D Struct. Biol. *74*, 519–530.

45. Pettersen, E.F., Goddard, T.D., Huang, C.C., Couch, G.S., Greenblatt, D.M., Meng, E.C., and Ferrin, T.E. (2004). UCSF Chimera-a visualization system for exploratory research and analysis. J. Comput. Chem. *25*, 1605–1612.

STAR★METHODS

KEY RESOURCES TABLE

REAGENT or RESOURCE	SOURCE	IDENTIFIER
Bacterial and virus strains		
E. Coli (MAX Efficiency DH10Bac)	ThermoFisher	10361012
Chemicals, peptides, and recombinant proteins		
n-Decyl-β-D-maltoside (DM)	Anatrace	D322LA
n-Undecyl-β-D-maltoside (UDM)	Anatrace	U300
Cholesteryl Hemisuccinate (CHS) tris salt	Sigma Aldrich	C6013
Complete EDTA-free Protease Inhibitor Cocktail	Roche	50 056 489 001
TEV protease	Produced in house	N/A
3C protease	Produced in house	N/A
PNGaseF	Produced in house	N/A
Critical commercial assays		
Talon Metal Affinity Resin	Takara Bio	635504
PD10 Desalting Columns	Cytiva	17-0851-01
Superdex 6 Increase 100/300 GL Column	Cytiva	29-0915-96
Deposited data		
TASK-1 pH 7.5 Atomic Coordinates	This paper	9G9V
TASK-3 pH7.5 Atomic Coordinates	This paper	9G9W
TASK-3 G236R pH7.5 Atomic Coordinates	This paper	9G9X
TASK-1 Coulomb Potential Maps	This paper	EMD-51158
TASK-3 Coulomb Potential Maps	This paper	EMD-51159
TASK-3 G236R Coulomb Potential Maps	This paper	EMD-51160
Experimental models: Cell lines		
Sf9 Insect cells	ThermoFisher	11496015
Oligonucleotides		
TASK-3 LIC forward TTAACAACCACAT ATACTATGAAGAGGCAGAACGTGCGG	This paper	N/A
TASK-3 LIC reverse TGAAATAACACC TCCAACTCTGCTTCAGCATCCCGCC GCTCATC	This paper	N/A
TASK-3 G236R forward GCTGACGGT CATCAGGGCCTTCCTCAACC	This paper	N/A
TASK-3 G236R reverse GGTTGAGG AAGGCCCTGATGACCGTCAGC	This paper	N/A
TASK-3 G236R LIC forward TTAAGAA GGAGATATACTATGAAGAGGCAGAA CGTGC	This paper	N/A
TASK-3 G236R LIC reverse GATT GGAAGTAGAGGTTCTCTGCGGCG AGGGATGCCCTCTC	This paper	N/A
TASK-3 G129D forward GTTCCAGAGCC TGGACGAGCGCATGAACAC	This paper	N/A
TASK-3 G129D reverse GTGTTCATGC GCTCGTCCAGGCTCTGGAAC	This paper	N/A
TASK-3 N133S forward GGCGAGC GCATGAGCACCTTCGTGCG	This paper	N/A
TASK-3 N133S reverse GCGCACGA AGGTGCTCATGCGCTCGC	This paper	N/A

(*Continued on next page*)

Continued

REAGENT or RESOURCE	SOURCE	IDENTIFIER
TASK-3 L241F forward GGGCCTTCC TCAACTTCGTCGTCCTCAGGTTC	This paper	N/A
TASK-3 L241F reverse GAACCTG AGGACGACGAAGTTGAGGAAGGCCC	This paper	N/A
Recombinant DNA		
pFB-CT10HF-LIC vector	Addgene	#39191
Functional expression plasmid pFAW	Sörmann et al.[11]	N/A
Software and algorithms		
SIMPLE	Caesar et al.[37]	https://simplecryoem.com/
CryoSPARC	Punjani et al.[38]	https://cryosparc.com/
RELION	Zivanov et al.[39]	https://relion.readthedocs.io/en/release-5.0/
UCSF pyem	Asarnow et al.[40]	https://github.com/asarnow/pyem
Cryosieve	Zhu et al.[41]	https://pypi.org/project/cryosieve/
Coot	Emsley et al.[42]	https://www2.mrc-lmb.cam.ac.uk/personal/pemsley/coot/
PHENIX	Adams et al.[43]	https://phenix-online.org/
ISOLDE	Croll[44]	https://tristanic.github.io/isolde/index.html
PyMOL	Schrodinger LLC	https://www.pymol.org/
USCF ChimeraX	Pettersen et al.[45]	https://www.cgl.ucsf.edu/chimera/
Other		
Vivaspin 20 100 kDa MWCO concentrator	Cytiva	28932363
Vivaspin 2 100 kDa MWCO concentrator	Cytiva	28932258
Quantifoil 300 Mesh Cu R1.2/1.3 Grids	Agar Scientific	AGS143-2-100
Au-Flat 300 Mesh Au R1.2/1.3 Grids	Molecular Dimensions	GF-1.2/1.3-3AU-45nm-50

EXPERIMENTAL MODEL AND STUDY PARTICIPANT DETAILS

Spodoptera frugiperda (Sf9) cells (Thermo Fisher Scientific, Cat. No. 11496015) were used for the expression of TASK-3 proteins. For large-scale protein expression, Sf9 cells were cultured in suspension at a density of 2 × 10^6 cells per mL. The cells were infected with baculovirus at a 5% virus ratio and incubated at 27°C for 72 h. Following infection, cells were harvested by centrifugation at 900 *g* for 10 min, frozen in liquid nitrogen, and stored at −80°C prior to purification.

METHOD DETAILS

Cloning and expression of TASK-3$^{Met1–Glu259}$ for structural studies

The human *KCNK9* gene (GenBank ID 51305), encoding the TASK-3 protein residues M1 to E259, was subcloned into a modified version of the pFB-CT10HF-LIC vector, containing a C-terminal HRV 3C protease site instead of the Tobacco Etch Virus protease site, but with the same decahistidine and FLAG tags.[18] This construct was used for WT TASK-3 expression. The TASK-3 G236R mutation was introduced with Quick Change Mutagenesis, and was subcloned into the pFB-CT10HF-LIC vector. The construct and comprised residues M1 to A265, and also contained a TEV protease site followed by a decahistidine tag and an FLAG tag. Baculoviruses were generated by transformation into DH10Bac cells and bacmid transfected into *Sf9* cells (Thermo Fisher Scientific) and amplified twice. Large scale expression was done by infecting Sf9 cells at a density of 2 × 10^6 cells per mL and a 5% virus ratio and grown at 27°C for 72 h. Cell were harvested by centrifugation at 900 × *g* for 10 min and frozen in liquid nitrogen and stored at −80°C prior to purification.

Purification of TASK-1 and TASK-3

TASK-1 and TASK-3^{G236R} proteins were purified as previously described for TASK-1,[18] with the exception that TASK-1 was purified in *n*-undecyl-β-*d*-maltopyranoside (UDM) (Anatrace) instead of *n*-decyl-β-*d*-maltopyranoside (DM). The UDM concentrations throughout purification were 1% w/v for solubilization, 0.09% for wash, elution and desalting buffers, and 0.045% for size exclusion buffer. The TASK-3 protein was purified by breaking the cells in 40 mL breaking buffer (50 mM HEPES pH 7.5, 200 mM KCl, 5% v/v glycerol) containing cOmplete EDTA-free Protease Inhibitor Cocktail (Roche) using an EmulsiFlex- C5 high-pressure homogenizer (Avestin). For solubilization, 1% DM and 0.1% CHS Tris salt was added and rotated for 1 h at 4°C. The solubilized fraction was

separated from cell debris by centrifugation at 35,000 *g* for 1 h at 4°C and the supernatant then collected. To collect the histidine tagged protein, 0.5 mL TALON resin (Takara Bio) per initial liter of cell culture was added, as well as imidazole at pH 8.0 to a final concentration of 5 mM. Following incubation for 1 h at 4°C, the Talon resin was collected and washed with 15 column volumes of wash buffer (50 mM HEPES pH 7.5, 200 mM KCl, 5% v/v glycerol, 20 mM imidazole pH 8.0, 0.24% w/v DM, 0.024% w/v CHS). The resin was transferred to a 15 mL centrifuge tube and the volume adjusted to 2 column volumes using wash buffer. Hexahistidine tagged HRV 3C protease and hexahistidine tagged PNGaseF were added to cleave the protein off the column, 150 μg and 50 μg per mL resin, respectively, and incubated for 16–20 h at 4°C. The flow through was collected and concentrated to 500 μL and injected onto a Superose 6 Increase 100/300 GL column (Cytiva) in gel filtration buffer (20 mM HEPES pH 7.5, 200 mM KCl, 0.12% w/v DM, 0.012% w/v CHS). Fractions containing TASK-3 were pooled and concentrated with a 100 kDa molecular weight cut off spin concentrator (Cytiva).

Cryo-EM grid preparation and data collection

For TASK-1 (3.6 mg mL^{-1}) and TASK-3 (8 mg mL^{-1}), 3 μL were adsorbed to glow-discharged holey carbon-coated grids (Quantifoil 300 mesh, Cu R1.2/1.3). were then blotted for 3 to 6 s at 100% humidity (4°C) and frozen in liquid ethane using a Vitrobot Mark IV (Thermo Fisher Scientific). Data were collected in counted superresolution bin 2 mode on a Titan Krios G3 (FEI) operating at 300 kV with a BioQuantum imaging filter (Gatan), and K3 direct detection camera (Gatan) at ×105,000 magnification, physical pixel size of 0.832 Å. Collection of TASK-1 data were conducted at a total dose rate of 41.173 $e^{-}/Å^2$ and 17,288 movies were collected in total. The grids used for collecting this TASK-1 data were prepared after adding 1.3 μM ONO-RS-082, a TASK-1 activator, but density corresponding to this small molecule activator could not be identified in the Coulomb potential map possibly due to the relatively low solubility of the compound and low final concentration that was used. The TASK-3 data were collected with a total dose of 39.56 $e^{-}/Å^2$ and 21,364 movies were collected in total. For TASK-3^{G236R} (6 mg mL^{-1}) the same process was conducted using holey gold grids (Au-Flat 300 mesh, R1.2/1.3, 45 nm gold film) with a total dose rate of 40.877 $e^{-}/Å^2$ and 20,627 movies.

Image processing

Initial micrograph processing of all three datasets was conducted using the SIMPLE pipeline,[37] using SIMPLE preprocess_stream for motion correction and patched contrast transfer function (CTF) estimation. Particles were picked from a subset of each dataset, and extracted in SIMPLE. All further processing was done in cryoSPARC.[38] Motion corrected micrographs were imported to cryoSPARC and CTF estimation was done. The initial particles extracted in SIMPLE were imported and subjected to 2D classification rounds and ab-initio reconstitution to yield a volume that templates for picking were generated. Particle repicking from the full dataset was done using the template picker within cryoSPARC. All further processing was done in cryoSPARC unless stated otherwise. For WT TASK-1, 8,116,956 particles were extracted and underwent one round of unmasked 2D classification, followed by four rounds of masked 2D classification and junk particles were removed. The resulting set of 1,076,556 particles were classified by five C1 ab initio classes and after heterogeneous refinement, three of these were selected for further processing. After one round of masked 2D classification, the remaining 680,017 particles were classified in three C2 ab initio classes. After heterogeneous refinement and homogeneous refinement of one class, the particles (358,967) were exported to RELION-5,[39] using the csparc2star.py script within UCSF pyem and subjected to Bayesian polishing. The polished particles were run through cryosieve[40] and particle stacks were imported back into cryoSPARC.[38] To find the highest resolution stack, each stack was subjected to one round of 2D classification, ab initio reconstruction in C1 followed by homogeneous and heterogeneous refinements, both in C2. The final particle set (117,627) yielded a map of 3.13 Å resolution, based on the FSC = 0.143 criteria. For TASK-3, 12,215,148 particles were initially extracted, which underwent two rounds of 2D classification. Subsequently, five C1 ab initio classes were generated from 1,904,926 particles. Following heterogeneous and non-uniform refinement, 597,895 particles were selected for further analysis. After 2D classification, ab initio reconstruction in C2 with five classes, and heterogeneous refinement applying C2 symmetry, one class with 286,131 particles was subjected to homogeneous and non-uniform refinements in C2. These particles were then exported to RELION and Bayesian polished, run through cryosieve and particle stacks were imported back into cryoSPARC, where they were processed as described above for TASK-1. The final C2 map from 93,760 particles was resolved to 3.32 Å. For TASK-3^{G236R}, 8,932,733 particles were extracted and subjected to one round of unmasked 2D classification, followed by five rounds of masked 2D classification, resulting in a set of 2,014,115 particles. These were sorted into five C1 ab initio classes and underwent heterogeneous refinement. Three classes, containing junk and lower resolution particles, were discarded and the remaining two were classified in 2D to remove further junk particles, resulting in a set of 1,145,364 particles. They were then classified into three C2 ab initio classes and after heterogeneous refinement, one class underwent heterogeneous refinement. These particles were Bayesian polished in RELION and narrowed down using cryosieve. Particle stacks were imported to cryoSPARC and went through 2D classification, ab initio reconstruction of one class in C1, and refinements in C2, as described for the TASK-1 map. The final particle set of 124,588 particles yielded a map at 2.48 Å.

Model building, fitting and refinement

Both TASK-3 models were manually built in the map on Coot to generate the initial model. After which the models were manually readjusted using COOT[42] and refined using *phenix.real_space_refine.*[3] For TASK-1, the X-ray crystal structure (PDB ID: 6RV2) was used as a starting model and manually fitted into the map in COOT. Final models were run through ISOLDE[44] and refined in phenix.real_space_refine using the generated ISOLDE models as references. Figures depicting structures were prepared using PyMOL (Shrodinger, LLC) or UCSF Chimera.[45]

Electrophysiology

The WT TASK-3 gene (*KCNK9*) was subcloned into a plasmid vector (pFAW) for *Xenopus laevis* oocyte transcription and expression. The mutations were introduced through site-directed mutagenesis and unless stated otherwise the two-electrode voltage-clamp recordings were performed as previously described.[11] Vector DNA was linearized with NheI or MluI and cRNA synthesized *in vitro* using the SP6 or T7 AmpliCap Max High Yield Message Maker Kit (Cellscript, USA) or HiScribe T7 ARCA mRNA Kit (New England Biolabs) and stored at −20°C. TEVC recordings were performed in *Xenopus laevis* oocytes at room temperature. Oocytes were injected with 1 ng of cRNA for WT or mutant TASK-3 and incubated for 2 days at 18°C. Microelectrodes were fabricated from glass pipettes, backfilled with 3 M KCl, and had a resistance of 0.2–1.0 MΩ. For inside-out patch-clamp recordings oocytes were incubated in a solution containing (mM): 54 NaCl, 30 KCl, 2.4 $NaHCO_3$, 0.82 $MgSO_4$ x7H_2O, 0.41 $CaCl_2$, 0.33 $Ca(NO_3)_2$ × 4H_2O and 7.5 TRIS (pH 7.4 adjusted with NaOH/HCl) for 1–7 days before use. Inside-out patch-clamp recordings were performed at room temperature with patch pipettes were made from thick-walled borosilicate glass with resistances of 0.3–0.5 MΩ (tip diameter of 15–25 μm) and filled with a pipette solution (in mM): 120 KCl, 10 HEPES and 3.6 $CaCl_2$ (pH 7.4 adjusted with KOH/HCl). Intracellular bath solutions and compounds were applied to the cytoplasmic side of excised patches via a gravity flow multi-barrel pipette system. Intracellular solution had the following composition (in mM): 120 KCl, 10 HEPES, 2 EGTA and 1 Pyrophosphate (pH adjusted with KOH/HCl). Currents were recorded and sampled at 10 kHz or higher and filtered with 3 kHz (−3 dB) or higher as appropriate.

QUANTIFICATION AND STATISTICAL ANALYSIS

The cryo-EM reconstruction and model building for TASK-1, TASK-3, and TASK-3 G236R were conducted using the procedures outlined in the detailed STAR methods section. The software packages used included SIMPLE, cryoSPARC, RELION, PYEM, Cryosieve, Coot, PHENIX and ISOLDE, as listed in the key resources table. Final model statistics are provided in Table S1. All graphs of functional data were generated using Origin 2016 (OriginLab Corporation, Northampton, MA). Bars represent mean ± SEM. Unless otherwise stated, unpaired Student's t test was used for statistical analysis, with $\alpha = 0.05$ as threshold of significance (*** = $p \leq 0.0001$). To minimize variability in recordings across different batches of oocytes, the recordings of mutant channels were normalized to the mean corresponding WT current from the same batch of oocytes. This allows the consistent comparison of the fold-change in current between the mutant and WT channel across different batches of oocytes. Every experiment was repeated at least on two different batches of oocytes to ensure reproducible and reliable results.